

Cross-correlation analysis of CMB with foregrounds for residuals

Pavan K. Aluri^{1*} and Pranati K. Rath,^{2†}

¹*Inter-University Centre for Astronomy and Astrophysics, Pune, India*

²*Institute Of Physics, Bhubaneswar, India*

Accepted XXX. Received YYY; in original form ZZZ

ABSTRACT

In this paper, we try to probe whether a clean CMB map obtained from the raw satellite data using a cleaning procedure is sufficiently clean. Specifically we study if there are any foreground residuals still present in the cleaned data using a cross-correlation statistic. Residual contamination is expected to be present, primarily, in the galactic plane due to the high emission from our own galaxy. A foreground mask is applied conventionally to avoid biases in the estimated quantities of interest due to foreground leakage. Here, we map foreground residuals, if present, in the unmasked region i.e., outside a CMB analysis mask. Further locally extended foreground-contaminated regions, found eventually, are studied to understand them better. The few contaminated regions thus identified may be used to slightly extend the available masks to make them more stringent.

Key words: cosmic microwave background - foregrounds - residuals - data analysis

1 INTRODUCTION

With the unprecedented measurements of the cosmic microwave background (CMB) temperature anisotropies, cosmology has plunged into a precision era (Bennett et al. 2003; Ade et al. 2014). This high resolution CMB data has been in turn used to probe some of the underlying assumptions of the standard cosmological model such as isotropy and non-gaussianity. Since the release of CMB data from WMAP’s first year observations (Bennett et al. 2003), many anomalous deviations from the standard model expectations have been reported (see Ref. Bennett et al. (2011, 2013); Ade et al. (2014, 2015) and the references there in). Some of these anomalies were studied in the context of foreground residuals that may still be present in the *clean* CMB maps, for example, in Slosar & Seljak (2004); Abramo, Sodre & Wuensche (2006); Bernui et al. (2012); de Oliveira-Costa & Tegmark (2006); Rakic, Rasanen & Schwarz (2006); Copi et al. (2007); Babich & Pierpaoli (2008); Gruppuso & Burigana (2009); Cabella et al. (2010); Short & Coles (2010); Aluri et al. (2011); Cruz et al. (2011); Aluri & Jain (2012); Lacasa et al. (2012); Chingangbam & Park (2013); Kovacs, Szapudi & Frei (2013); Liu, Mertsch & Sarkar (2014); Novaes et al. (2014); Rassat et al. (2014); Axelsson et al. (2015).

Along with the cosmic signal of our interest, a CMB

detector would register all the microwave emission including emission from our own galaxy and extragalactic sources that compromises the CMB observations. As such the raw maps are *cleaned* using a variety of procedures (Tegmark, de Oliveira-Costa & Hamilton 2003; Eriksen et al. 2004; Leach et al. 2008; Saha 2011). Ideally the aim of every cleaning procedure is to completely remove any trace of foregrounds from the raw data and obtain the pristine cosmic signal. However in practice due to high foreground emission in some regions of the sky including the galactic plane, the recovered CMB signal still remains contaminated in those parts of the sky. To avoid spurious inferences from the bias thus induced, for example in obtaining the angular power spectrum or cosmological parameters there off, a cleaned CMB map is masked omitting regions of the sky where the recovered CMB is unreliable. The quantities of interest are thus estimated from the unmasked region.

In this paper, we study a clean CMB map for foreground residuals that may still be present in it, even after employing a foreground mask. Since the foreground emission is strong in some regions of the CMB sky, a suitable mask (a common mask or a frequency specific mask) is devised to eliminate pixels beyond a chosen threshold level (Tegmark, de Oliveira-Costa & Hamilton 2003; Bennett et al. 2003). No significant foreground residuals are expected to be present outside a mask such as the *KQ75* mask used in the NASA’s WMAP nine year data analysis (Bennett et al. 2013). Further, we will probe any anomalous regions thus identified, if

* E-mail: aluri@iucaa.ernet.in

† E-mail: pranati@iopb.res.in

they were earlier reported in the CMB literature and thus have already drawn some interest.

Here we make use of a cross-correlation statistic to probe foreground residuals, that quantifies the level of correlation between a clean CMB map and a foreground template. This correlation coefficient is computed outside a galactic mask. A cross-correlation analysis of CMB data with external data sets was already used in the literature in a variety of ways, for example, in Afshordi, Loh & Strauss (2004); Coles et al. (2004); Dineen & Coles (2004); Bernardi et al. (2005); Naselsky et al. (2005); Alvarez et al. (2006); Rasat et al. (2007); Land & Slosar (2007); Sarkar, Datta & Bharadwaj (2009); Hernandez-Monteagudo (2010); Lopez-Corredoira, Labini & Betancort-Rijo (2010); Naselsky et al. (2010); Sawangwit et al. (2010); Ilic et al. (2011); Taburet et al. (2011); Hansen et al. (2012); Wibig & Wolfendale (2015).

The paper is organized as follows. In section 2, we will introduce the cross-correlation statistic used for probing foreground residuals that may still be present outside a chosen mask. Then in section 3, the data sets used for foreground templates, clean CMB map and foreground mask, and preparation of simulations to complement the observed data, are discussed. In section 4, the statistic is applied to the data and regions that are significantly correlated with the foreground templates are mapped out. Further we carry out a local analysis of regions of anomalous correlation, that were found in earlier studies and have received significant attention. Finally a brief discussion and conclusions are presented in section 5.

2 CROSS-CORRELATION STATISTIC

We employ a cross-correlation coefficient (CCC) that would map the correlations between a clean CMB map and a foreground template in small patches over the entire sky. It is defined to identify regions containing anomalous foreground residuals outside a foreground mask. Using the HEALPix sky discretization scheme, we define the CCC as (Aluri 2011)

$$\mathcal{R}(P) = \frac{\sum_{p \in P} [T(p) - \bar{T}(P)] [F(p) - \bar{F}(P)]}{\sqrt{\sum_{p \in P} [T(p) - \bar{T}(P)]^2 \sum_{p \in P} [F(p) - \bar{F}(P)]^2}}, \quad (1)$$

where P corresponds to a pixel in a lower resolution (lower N_{side}) HEALPix grid that is used as mask on a high resolution (higher N_{side}) CMB map, $T(p)$, and foreground template, $F(p)$, whose pixels are indexed by p . So, the correlation coefficient between a CMB map and a foreground is computed using all the pixels p in the input maps, falling in the region covered by the upgraded larger pixel from a lower N_{side} HEALPix grid (upgraded to the same HEALPix resolution as input maps). The CCC thus computed is associated with the pixel P of the low resolution HEALPix grid to obtain an all sky map of the correlations between cleaned CMB data and foregrounds. The local means, $\bar{T}(P)$ and $\bar{F}(P)$, of the CMB map and foreground templates are also obtained from the pixels $p \in P$ of the same larger pixel region from the low resolution HEALPix grid at which we are mapping the correlations.

To illustrate, for input clean CMB and foreground maps at HEALPix resolution of $N_{side} = 512$, we may choose a lower

resolution HEALPix grid of $N_{side} = 16$ to robustly map the correlations between the input maps. So, the CCC is computed using a total of $(512/16)^2 = 1024$ pixels of the input maps that fall into the same large pixel region corresponding to the low resolution HEALPix $N_{side} = 16$ grid.

Since we would map the entire sky, we downgrade the high resolution foreground mask with $\{1,0\}$'s to the same N_{side} as the CCC map. Further we exclude the pixels which are not *one*, meaning pixels that are at the edge of the mask and didn't form a whole pixel at the lower resolution are excluded.

However, since a HEALPix tessellation is made of disjoint pixels, some of the anomalous regions may be cut-in, and would return a cross-correlation coefficient that spuriously depicts it as insignificant. So, we use a circular disk of a chosen radius centered at each pixel of a chosen HEALPix grid to continuously scan the input maps and compute the CCC. It is then associated with that central pixel about which the circular disc mask is defined to obtain a CCC map between CMB and foregrounds. The CCC map is obtained at a lower resolution than the input maps for convenience of computation but nevertheless maps the correlations sufficiently smoothly. This circular disc is taken in union with a foreground mask so that pixels in the region circumscribed by the circular disc which are flagged as contaminated by the foreground mask does not contribute to the CCC statistic being computed. Such a union will result in less number of pixels being available for computing the statistic.

In order to have a robust estimate of the CCC statistic, we compute the CCC only if atleast 80% of the pixels are retained in the union of the foreground mask and circular disc centered at any pixel of the chosen HEALPix grid for obtaining the CCC map. The local means $\bar{T}(P)$ and $\bar{F}(P)$ are also computed using only the unmasked pixels in the effective circular disc. If the 80% criteria is not satisfied in a local effective circular mask at any sky location compared to the full disc, it is deemed invalid. In practice, we set these invalid pixels to HEALPix bad/missing pixel value of -1.6375×10^{30} . Further we can take the means \bar{T} and \bar{F} to correspond to those of the respective full maps outside the foreground mask, so that we would be considering deviations with respect to the full map means. Thus our statistic of Eq. [1], would be same as that of Hansen et al. (2012). In this paper, we would be using this version of the statistic.

Again, to illustrate, for an input CMB map and a foreground template at $N_{side} = 512$, we can compute the CCC map at $N_{side} = 128$, for example, to smoothly map the correlations between them. Using a circular disc mask of radius 5° (degrees), for example, at each sky location in union with a foreground mask, we would be using atleast ≈ 4792 pixels of the input maps wherever available, as explained later. If these many are not available, the corresponding pixel of CCC map is set to HEALPix bad value.

3 DATA SETS AND SIMULATIONS

3.1 Observational data used

In this work, we use the WMAP's nine year ILC map (WILC9 hereafter) (Eriksen et al. 2004; Bennett et al. 2013) as the cleaned CMB map to probe foreground residuals. As

described later, we would be using a sufficiently extended mask to omit regions where the recovered CMB signal is unreliable. So, CMB sky obtained using any of the cleaning procedures are expected to be in agreement with each other outside a foreground mask. The WILC9 map is available at HEALPix $N_{side} = 512$ with a resolution of Gaussian beam $fwhm = 1^\circ$.

For galactic foreground templates, we use the thermal dust template at 94 GHz (Finkbeiner, Davis & Schlegel 1999), $H\alpha$ map that is used as proxy for galactic free-free emission (Finkbeiner 2003), and the 408 MHz Haslam map dominated by synchrotron emission from our galaxy (Haslam et al. 1982). These independent foreground emission templates are used by WMAP as well as PLANCK teams as priors in their foreground component estimation/separation methods¹ (Bennett et al. 2013; Adam et al. 2015a). Here after we refer to these foreground templates as FDS, $H\alpha$ and Haslam maps respectively. Eventually, we will also make use of the foreground maps obtained using the CMB observations from ESA’s PLANCK satellite to study local anomalous regions. We specifically use the galactic thermal dust, free-free and synchrotron maps estimated using the Commander algorithm that are part of the PLANCK’s 2015 data release² (Adam et al. 2015a). As these foreground maps are obtained from a completely different mission with different noise and systematics, they would complement the three foreground templates mentioned above, unlike the MEM or MCMC derived foreground maps from WMAP data itself³ (Bennett et al. 2013).

Since the original HEALPix resolution and beam smoothing of the individual maps are different, we downgrade them to a common HEALPix $N_{side} = 256$ and to have a resolution of 1° FWHM Gaussian beam. All the analysis presented in this work is carried out using data maps, foreground mask and simulations at $N_{side} = 256$. The cross-correlation coefficient (CCC) map and its significance map are obtained at $N_{side} = 128$.

As a foreground mask, we use the WMAP’s nine year $KQ75$ extended temperature mask which has an unmasked sky fraction of $f_{sky} \approx 0.688$. However, the $KQ75$ mask is available at $N_{side} = 512$. In order to obtain a suitable mask at $N_{side} = 256$ where we perform all the analysis, the $KQ75$ is first inverted ($\{1,0\} \rightarrow \{0,1\}$ respectively). The inverted mask is then downgraded to $N_{side} = 256$, and smoothed with a Gaussian beam of $fwhm = 1^\circ$ (degree) which is same as the beam resolution of the observed maps. A cutoff of 0.01 is imposed on the inverted, downgraded, smoothed mask so as to extend it to handle leakage of foregrounds due to smearing of extended and point sources due to beam smoothing and downgrading of the observed maps which are available at higher N_{side} . Some of the island pixels are also removed before inverting it to get a reliable $\{1,0\}$ foreground mask at $N_{side} = 256$. The mask thus obtained and used throughout



Figure 1. Shown here is the foreground mask we use in the present analysis which is at $N_{side} = 256$ and has an available sky fraction of $f_{sky} \approx 0.530$. Yellow and black regions denote the unmasked and masked parts of the sky, respectively. It is obtained by suitably processing and extending the $KQ75$ mask used by the WMAP science team in their nine year analysis. See text for details. [color version online]

our analysis is shown in Fig. [1], which has an unmasked sky fraction of $f_{sky} \approx 0.530$.

3.2 Preparing the simulations

To complement the observed CMB maps and compute significances of the observed correlations, we generate an ensemble of WILC9-like maps. We do so as follows.

First, we simulate a set of 1000 isotropic, Gaussian CMB realizations based on a best fit theoretical angular power spectrum (C_l). The best fit C_l are obtained using WMAP’s nine year cosmological parameters (Hinshaw et al. 2013) as input to Code for Anisotropies in the Microwave Background (CAMB)⁴ (Lewis, Challinor & Lasenby 2000; Howlett et al. 2012). Each random realization is convolved with beam transfer functions (b_l) corresponding to each of the five WMAP channels⁵ to create five beam smoothed maps. These convolved maps are then added with anisotropic frequency specific detector noise simulated using the noise rms (σ_0) corresponding to each observed frequency band map, and the effective number of observations in each pixel/sky direction ($N_{obs}(p)$). The effective noise rms in a pixel ‘ p ’ of the measured anisotropies at a frequency band ‘ i ’ is given by $\sigma^i(p) = \sigma_0^i / \sqrt{N_{obs}^i(p)}$. The σ_0 values and N_{obs} maps are also provided by the WMAP team with the nine year data release⁶. Thus we simulate random Gaussian noise maps using $\sigma^i(p)$ corresponding to the WMAP’s 23(K), 33(Ka), 41(Q), 61(V) and 94(W) GHz channels.

In this way, five sets of 1000 mock WMAP nine year observed maps were generated with appropriate channel specific beam and noise properties. To obtain an ILC-like map, we deconvolve each of the mock channel maps with the respective beam window functions, and smooth them with a Gaussian beam of $fwhm = 1^\circ$. Now, we co-add the smoothed WMAP-like channel maps using smoothed noise variance maps to obtain WILC9-like maps. So, we treated the covariance matrix to be essentially diagonal, and used

¹ All these three foreground templates are publicly available from the NASA’s Legacy Archive for Microwave Background Data Analysis (LAMBDA) web page : <http://lambda.gsfc.nasa.gov/>.

² PLANCK’s public release 2 data is available at <http://irsa.ipac.caltech.edu/Missions/planck.html>.

³ <http://lambda.gsfc.nasa.gov/>

⁴ The code is available for public download at <http://camb.info/>.

⁵ <http://lambda.gsfc.nasa.gov/>

⁶ <http://lambda.gsfc.nasa.gov/>

the smoothed noise variance maps themselves as weights for taking the linear combination⁷. These maps are then downgraded to $N_{side} = 256$. Thus we generated a set of 1000 ILC-like CMB maps at $N_{side} = 256$. In the next section we proceed with the analysis of observed maps and estimate significances using these simulations.

4 ANALYSIS AND RESULTS

4.1 Foreground residuals in a clean CMB map

In this section, we probe the presence of residual foregrounds, if any, in the WMAP's nine year ILC cleaned CMB map (WILC9) by cross-correlating it with the foreground templates of thermal dust, free-free and synchrotron emission from our own galaxy.

We apply our cross-correlation coefficient (CCC) statistic defined in Eq. [1] to obtain a CCC map with each foreground at $N_{side} = 128$. The input WILC9 map and a foreground template at $N_{side} = 256$ are scanned continuously using circular discs of radii $1^\circ, 2^\circ, 3^\circ, 4^\circ, 5^\circ$ and 6° (degrees). This is done in union with the foreground mask at $N_{side} = 256$ derived from WMAP's nine year *KQ75* mask, with the additional constraint of having at least 80% of usable pixels in the effective circular mask, compared to the full disc mask of a chosen radius. This is to ensure a robust computation of the CCC at a chosen location on the sky. By using a circular disc of radius 1° , and demanding availability of at least a fraction of 0.8 number of pixels in the net disc mask after combining with the foreground mask, we will be using at least ≈ 48 pixels for computing the CCC at any location of the sky (treating each pixel of an $N_{side} = 256$ map as a square, it would have a size of $a = \sqrt{4\pi/(12 \times 256^2)} \times 180^\circ 60'/\pi = 13.74'$ (arcmin) resulting in demanding availability of at least $0.8 \times \pi r_{disc}^2/a^2 \approx 47.9$ pixels). Likewise we will be using at least $\approx 192, 431, 767, 1198$ and 1725 pixels to compute CCC when using circular discs of $2^\circ, 3^\circ, 4^\circ, 5^\circ$ and 6° (degrees) radii, where ever the desired constraint is satisfied locally on the sky.

To begin with the analysis, we test the level of correlation between two clean CMB maps viz., WMAP's nine year ILC map and the CMB map from PLANCK's 2015 data estimated using the Commander algorithm (Eriksen et al. 2008; Adam et al. 2015b). Their cross-correlation map is shown in the *left* plot of Fig. [2]. We choose a filter disc radius of 3° to

obtain this CCC map at $N_{side} = 128$. Also shown in Fig. [2] (*right*) is a histogram of the pixels of this CCC map. It is readily evident that the two clean CMB maps from different missions are highly correlated, as expected, with most of the coefficients across the sky closer to 'one'. Since we take the union of a circular disc with the foreground mask shown in Fig. [1], with a further constrain of having at least 80% of the pixels in the net circular disc, the net sky over which CCC is computed is smaller than the foreground mask itself ($\approx 32\%$ of the whole sky). The grey pixels didn't satisfy these constraints and are left out of the analysis. Thus, if any foreground residuals are found eventually, we are warranted of (still) using the WILC9 map to probe foreground residuals in cleaned CMB data.

Moving towards the main analysis, we now correlate the WILC9 clean CMB map with foreground templates viz., FDS map for thermal dust, $H\alpha$ for free-free, and Haslam map for synchrotron emissions from our own galaxy. The input CMB and foreground maps are at HEALPix $N_{side} = 256$, and the output correlation maps are obtained at $N_{side} = 128$. The resulting CCC maps are shown in Fig. [3]. Circular disc masks of 1° to 6° (degrees) radii are used at each sky position, in steps of one degree, to filter the residual foregrounds by angular size. However the results are shown corresponding to the disc masks of size 2° to 5° (degrees) radii, only, in Fig. [3]. The local circular disc masks are used in conjunction with the suitably modified *KQ75* mask from WMAP nine year data shown in Fig. [1]. By demanding the availability of at least 80% of pixels in the net circular mask compared to the full disc at any location on the sky, the correlations are mapped over a fraction of $\approx 0.45, 0.38, 0.32, 0.31, 0.30$ and 0.29 of the sky, for our chosen disc masks of radii $1^\circ, 2^\circ, 3^\circ, 4^\circ, 5^\circ$ and 6° (degrees) respectively.

One should be warned of directly drawing inferences from the CCC maps of Fig. [3], as there are regions of apparent high correlation and anti-correlation between the clean CMB map and foregrounds, as indicated by the color scaling used. In order to quantify their significance, we obtain p -maps corresponding to each of the correlation maps between clean CMB data and foregrounds. p -maps are maps of p -values for each valid pixel at any location of the sky at which CCC is computed between WILC9 CMB map and foreground templates. So they too span the same sky region and have the same N_{side} as the observed correlation maps shown in Fig. [3]. The p -maps are obtained by correlating the foreground templates with the isotropic, Gaussian simulations described in section 3. All the simulated 1000 WMAP nine year ILC-like maps are correlated with the thermal dust, free-free and synchrotron foreground templates, and the *probability to exceed* the observed correlation in the data at each valid pixel of the CCC maps is computed. This p -value is then associated with a pixel of same index to obtain a p -map corresponding to a data CCC map. However, to identify the anomalous regions with significant foreground contamination, we chose a cutoff p -value exceeding which we retain that pixel in the p -map. The p -maps thus obtained are shown in Fig. [4] for a cutoff p -value of 0.02 (i.e., a random chance occurrence probability of 2% or less).

As expected, the p -maps are largely empty. However they reveal that there are still few extended regions of significant contamination. With smaller disc mask radius there are many stray or small island pixel regions which were found

⁷ Alternatively, one can use the same weights used for linearly combining the WMAP nine year smoothed raw maps to get the ILC CMB map. This should be done iteratively over all the 12 sky partitions in the same way as the observed maps were combined to obtain a composite clean CMB map. Since the simulations used are independent random realizations of the observed sky, the statistical independence of the resultant ILC-like maps would still be intact, despite using fixed weights for linearly combining them. This way we can bypass the ambiguity over the uncertainty regarding the use of inverse variance weighing to combine the smoothed band maps, rather than using the inverse of the full noise covariance matrix. Further we will be truly mimicking the iterative cleaning employed in ILC procedure. The iterative cleaning is used to deal with different levels of foreground emission in various parts of the CMB sky by choosing appropriate weights suitable for that region of the sky.

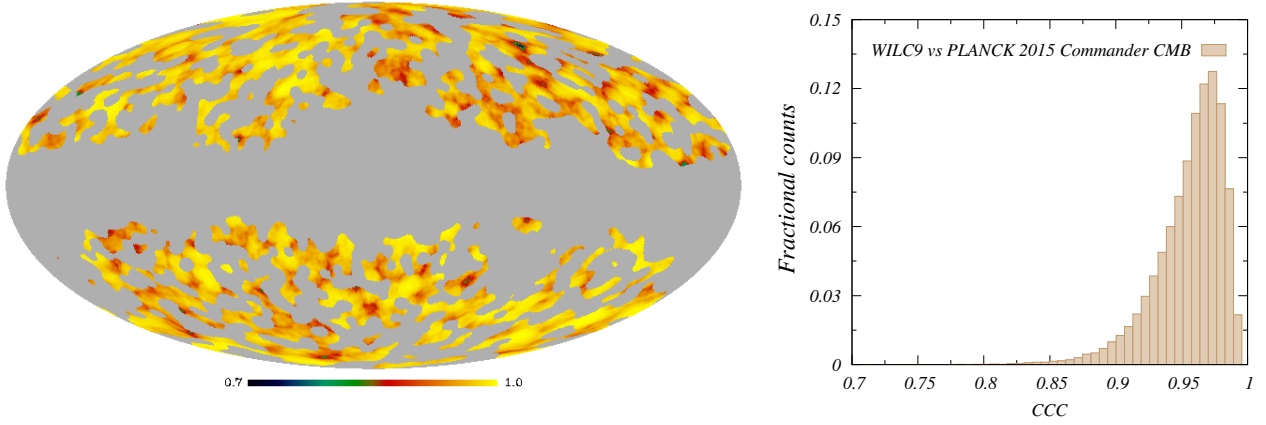


Figure 2. *Left:* The correlation map of clean CMB maps obtained from two different missions viz., WMAP’s nine year ILC map (WILC9) and the PLANCK’s 2015 Commander CMB map, using a filter disc radius of 3° (degrees) at $N_{side} = 128$ is shown here. As expected both of them are highly and positively correlated across the sky. *Right:* Histogram plot of all the correlation coefficients from the CCC map shown to the left. We readily see that the two maps are well correlated as expected. A total of 62721 pixels are valid, out of the $12 \times 128^2 = 196608$ pixels of an $N_{side} = 128$ map ($\approx 32\%$ of the sky), in the CCC map shown to the left. The histogram plot is made by sorting these valid pixels into 50 bins. [color version online]

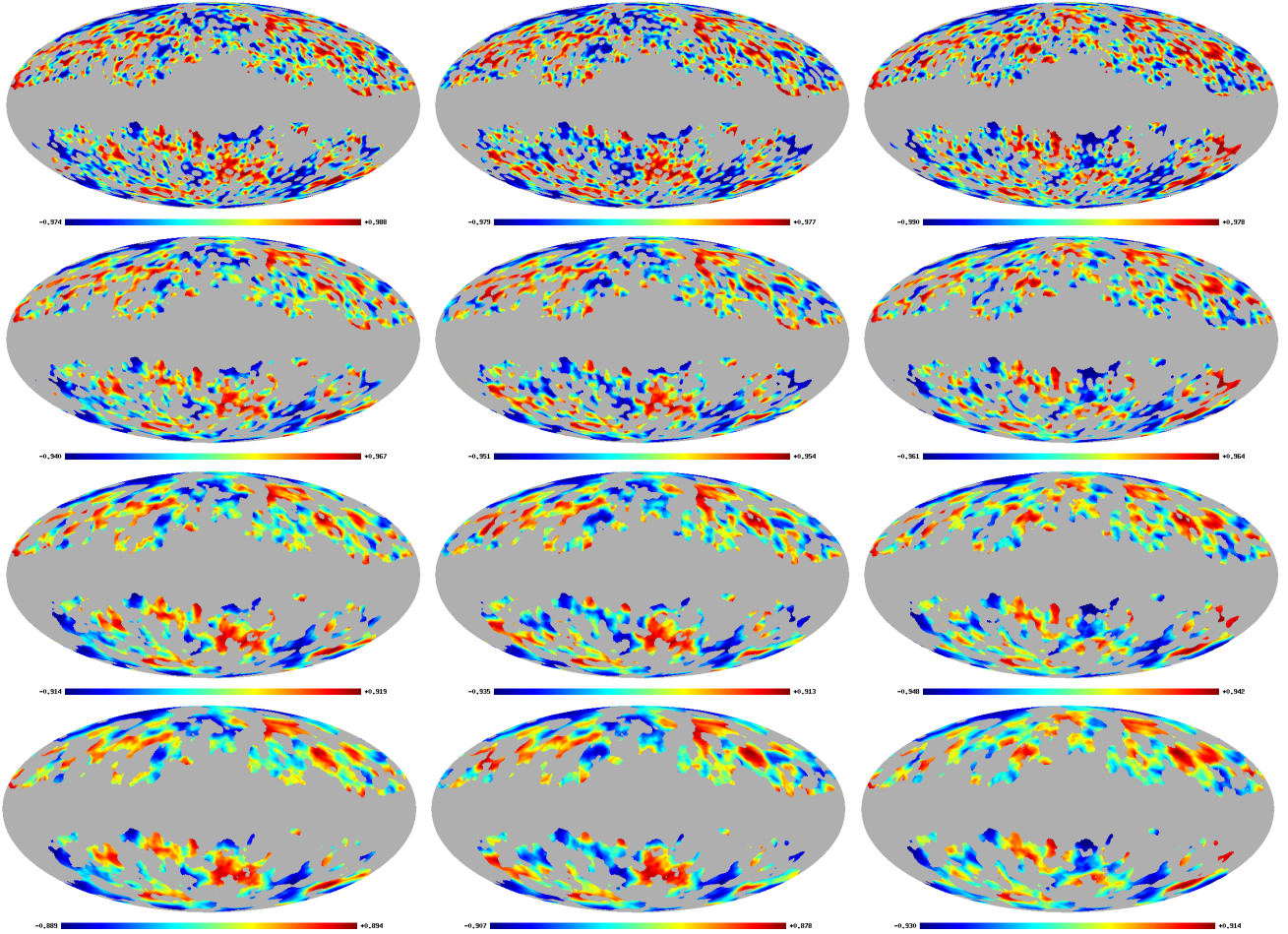


Figure 3. Correlation maps of WMAP’s nine year ILC map with the foreground templates FDS thermal dust map (*first column*), $H\alpha$ map (*second column*), and the Haslam’s 408 MHz map (*third column*) are presented here. The CCC maps obtained using circular disc masks of radii 2° , 3° , 4° , and 5° (degrees) are shown from *first* to *fourth* row, respectively. [color version online]

to be anomalous along with some extended patches. But, using larger discs for probing the residuals, only relatively extended or blob like regions remain. In Fig. [4], we have again shown only the p -maps for circular discs of radii 2° to 5° (degrees), corresponding to those of Fig. [3]. With 1° (degree) radius circular disc, there are many stray and few pixel islands, which may be arising due to its smaller disc size that allows the use of only $\pi(60')^2/(13.74')^2 \approx 60$ pixels at best to compute the CCC locally. Among these already few pixels there may be an unresolved point source or some may be sitting on the edge of the foreground mask used. Using disc of angular size 6° , the anomalous regions are similar to those from using the 5° circular mask, if not for some stray pixels/islands. Hence these results are not shown for brevity.

We also checked the p -maps with a cutoff of 0.01 (i.e., 1% or less probability to exceed the observed data correlation). Except for the disappearance of stray/island pixels, the p -value maps essentially look the same. The same extended regions still remain anomalously correlated with the foregrounds.

We notice that, with disc masks of larger radii, extended regions of anomalous correlation are found in CCC maps with thermal dust and synchrotron templates and, not so, relatively, with the free-free template. This may be due to the fact that free-free does not dominate at any of the frequency channels, in the same way as the galactic synchrotron and thermal dust emissions, in which WMAP made the observations. Next, we will locally analyze interesting extended regions of anomalous correlation.

4.2 Local analysis of anomalously correlated regions : CMB cold spot

In this section, we locally probe the extended anomalous regions with significant foreground correlation found in the previous section. Among the identified regions with spurious foreground contamination, we study the *cold spot* region. Cold spot is an anomalously low temperature region found in CMB sky in the direction $(l, b) = (209^\circ, -57^\circ)$, in galactic co-ordinates, with an angular size of $\approx 10^\circ$ (Vielva et al. 2004). Since its detection, the CMB cold spot received significant attention in the literature (Bennett et al. 2011; Ade et al. 2014, 2015; Naselsky et al. 2010; Tomita 2005; Cruz et al. 2006; Inoue & Silk 2007; Rudnick, Brown & Williams 2007; Cruz et al. 2008; Bernui 2009; Smith & Huterer 2010; Zhang & Huterer 2010; Afshordi, Slosar & Wang 2011).

From the CCC analysis of the previous section, we find that the cold spot region of WILC9 CMB map is well correlated with the FDS (thermal dust) and 408 MHz Haslam (synchrotron) maps. So we probe the cold spot region locally using a $10^\circ \times 14^\circ$ square mask, and estimate the CCC and its significance from that region as a whole. This square patch mask in union with the foreground mask of Fig. [1] is shown in Fig. [5] (*left*). Also shown in Fig. [5], are the CMB cold spot region itself from WILC9 map (*second*), and the p -map's of CMB correlation with FDS dust and 408 MHz Haslam map (*third* and *fourth*) shown in Fig. [4], corresponding to using 3° radius circular disc masks but centered towards the cold spot direction.

Using this square patch mask, we compute the correlation coefficient defined in Eq. [1], between CMB and three foreground templates. For completeness, we include

the free-free template also in this local analysis. Complementing the FDS thermal dust map, 408 MHz Haslam's synchrotron map, and $H\alpha$ map for free-free emission, we also make use of the all sky foreground maps from PLANCK 2015 data release, estimated using the Commander algorithm⁸ (Finkbeiner, Davis & Schlegel 1999; Finkbeiner 2003; Haslam et al. 1982; Adam et al. 2015a). Since they are derived from a completely different mission with different systematics and noise, they would augment the independent templates used so far, in a way not possible with the MEM and MCMC estimated foreground maps from WMAP data itself (Bennett et al. 2013).

The CCC from the cold spot region obtained using the square mask is compared with 1000 coefficients, computed by correlating 1000 WILC9-like CMB realizations with the three independent foreground templates as well as with the PLANCK 2015 data derived foreground maps. So, instead of a local circular disc mask as used in the previous section, a fixed square mask is used to do this local correlation analysis of cold spot region as a whole. In Fig. [6], we show the distribution of CCC from the correlation of simulated CMB skies with the six foreground templates in the cold spot region only, using the square mask. The observed CCC values are also denoted, by a *filled square* and a *filled circle* point types corresponding to two templates used for each foreground emission type. As expected we see that the CCC with $H\alpha$ map (*middle* plot) is not anomalous with a p -value= 0.172. The cold spot CCC of WILC9 CMB map with FDS thermal dust is found to be anomalously correlated with a p -value=0.046, that is outside 95% confidence level. However, the cold spot CCC of our clean CMB map with Haslam map turns out to be insignificant with a p -value= 0.254. It is also readily evident that the significances using PLANCK 2015 Commander estimated thermal dust, free-free and synchrotron maps are similar to the CCC significances using independent foreground templates viz., FDS, $H\alpha$ and Haslam maps. The p -values of cold spot CCC with the PLANCK 2015 data derived foregrounds are found to be $p = 0.048, 0.128, 0.153$, respectively.

The significance found for the cold spot CCC of the clean CMB map with synchrotron template is puzzling, despite what is suggested by p -map from that region shown in Fig.[5] (*fourth*). From Fig.[5], the p -values contour for correlation with synchrotron (*fourth* figure) can be seen to be smaller than that with thermal dust (*third* figure). So, when we are using a square patch mask of the same size to probe the cold spot region as a whole, the significance of correlation with synchrotron is less because it contains less anomalously correlated/contaminated pixels in it compared to the thermal dust.

5 CONCLUSIONS

In summary, in this paper we tried to investigate the presence of foreground residuals that may still be present in a *cleaned* CMB map after foreground reduction. To that extent we carried out a correlation analysis of WMAP's nine year ILC CMB map (WILC9) with three independent

⁸ <http://irsa.ipac.caltech.edu/Missions/planck.html>

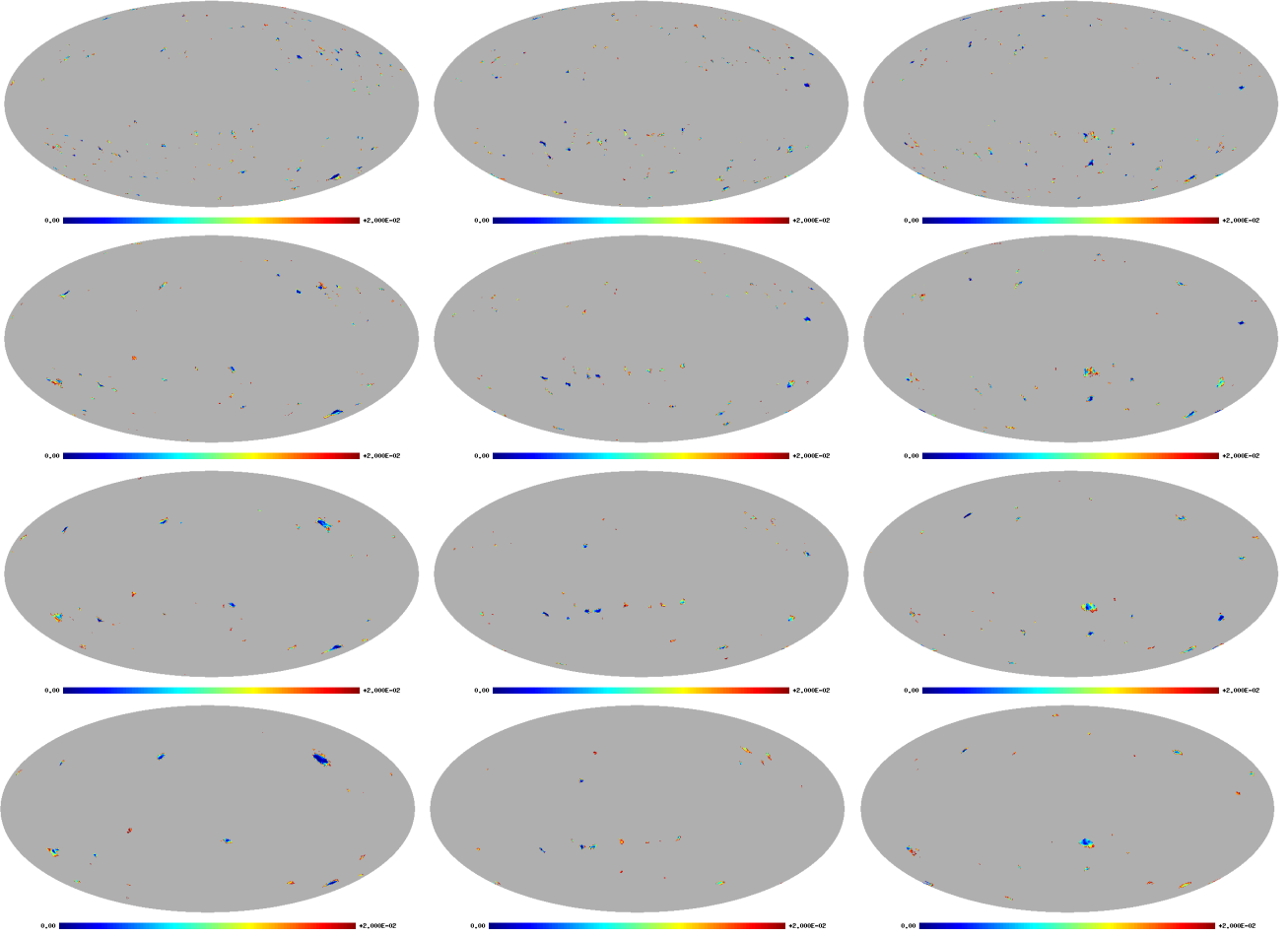


Figure 4. p -value map's of correlations of WILC9 CMB map with foreground templates viz., FDS thermal dust, $H\alpha$, and the Haslam maps are shown here corresponding to those presented in Fig. [3]. Only those regions which are anomalous with a *probability to exceed* by $p = 0.02$ i.e., a 2% or less by a random chance are highlighted. One can readily see that the p -maps are almost empty. There are only few regions with significant residual contamination, as expected. [color version online]

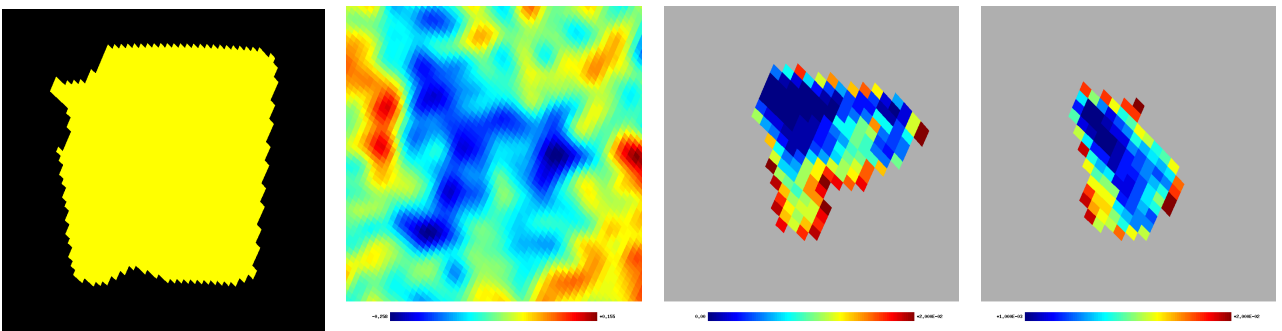


Figure 5. *First:* A square mask of size $10^\circ \times 14^\circ$, that is used to further probe the local anomalous region of CMB cold spot, is shown here. Yellow and black denote unmasked (1) and masked (0) regions of the square mask. *Second:* The CMB cold spot region from the WMAP's nine year ILC map at $N_{side} = 256$ is shown here. The extended blue feature (approximately 10° in angular size in the direction $(l, b) = (209^\circ, -57^\circ)$, in galactic coordinates) is the cold spot region. *Third and Fourth:* The p -maps of CMB correlation with the thermal dust and synchrotron templates, respectively, obtained using a local filter disc radius of 3° are presented here. They are same p -maps shown in Fig. [4], but are shown centered in the cold spot direction shown to the left. [color version online]

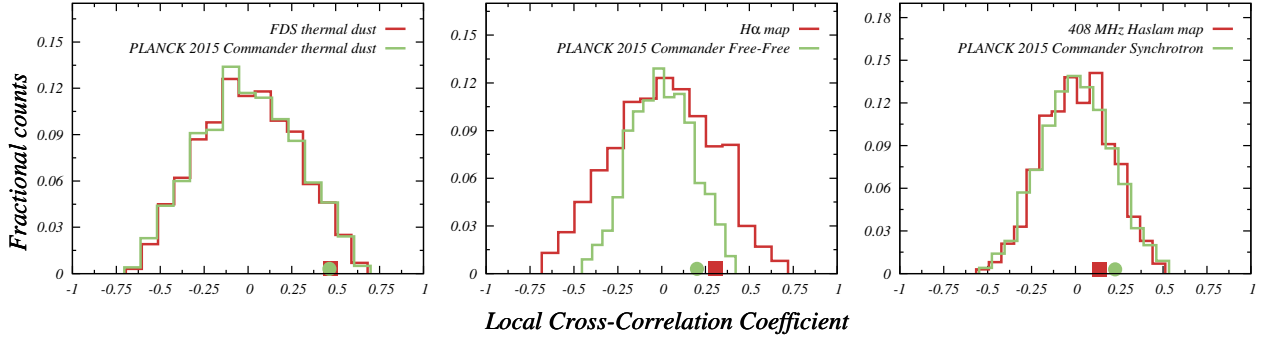


Figure 6. Histogram plots corresponding to local correlation analysis of WILC9 map in the direction of cold spot region using the square patch mask shown in Fig. [5] with six foreground templates, is presented here. Independent foreground templates for galactic thermal dust (FDS map), synchrotron (Haslam map), and free-free ($H\alpha$ map) emissions, along with foreground maps provided with the PLANCK 2015 data release for the same three emission types are used here. The filled *red square* and *green circle* denote observed CCC from the cold spot region when correlated with independent and PLANCK 2015 data derived foreground maps, respectively, used for each emission type. [color version online]

foreground templates corresponding to the three dominant galactic emissions viz., thermal dust (FDS map), free-free ($H\alpha$ map) and synchrotron (408 MHz Haslam map). The correlations are mapped out over the entire sky using a local circular disc mask of different radii at each sky location to filter anomalous residuals by angular size. The local circular disc masks are taken in union with the suitably modified $KQ75$ temperature mask used in WMAP nine year data analysis. This way we will be probing foreground residuals only in the supposedly clean regions of the foreground reduced CMB map. Cross-correlation coefficients (CCCs) are computed at pixels/sky directions which have atleast 80% of pixels in the net circular mask after combining with foreground mask, compared to the full disc mask of a chosen radius.

The CCC maps of CMB with foreground templates are computed at $N_{side} = 128$ with input CMB and foreground maps at $N_{side} = 256$. Local circular disc masks of different radii, viz., 1° , 2° , 3° , 4° , 5° and 6° (degree), are used to identify foreground residuals by angular size. A set of 1000 WMAP nine year ILC-like CMB skies are simulated to complement the data used and find significances of the observed anomalously contaminated regions.

Although, the CCC maps are largely empty, few regions with spurious correlations were found. Some of the extended regions are persistent even with the largest (6° radius) circular disc mask used for filtering. A curious correlation is found in the CMB cold spot region between WILC9 map and the thermal dust and synchrotron templates. With this finding, the cold spot region is further studied by performing a local correlation analysis using a fixed square mask of size $10^\circ \times 14^\circ$ encompassing the cold spot region. The CCC of CMB with FDS thermal dust map from the cold spot region as a whole using the square mask is found to be anomalous by more than 95% confidence level. However the cold spot CCC with synchrotron is found to be insignificant in this local analysis using square mask. It could be due to less number of contaminated pixels in the chosen square region due to synchrotron compared to thermal dust.

This analysis may be used to include the few contaminated regions found here with the usual foreground masks to make them more robust.

ACKNOWLEDGEMENTS

We acknowledge the use of the NASA’s Legacy Archive for Microwave Background Data Analysis (LAMBDA), as well as ESA’s PLANCK Legacy Archive (PLA) in the present work. We also acknowledge extensive use of HEALPix software package in this work.

REFERENCES

- Bennett C. L. et al., 2003, ApJS, 148, 1
Ade P. A. R. et al., 2014, A&A, 571, A1
Bennett C. L., et al., 2011, ApJS, 192, 17
Bennett C. L., et al., 2013, ApJS, 208, 20B
Ade P. A. R. et al., 2014, A&A, 571, A23
Ade P. A. R. et al., 2015, arxiv:1506.07135
Slosar A., and Seljak U., 2004, PRD, 70, 083002
Abramo L. R., Sodre L. Jr., and Wuensche C. A., 2006, PRD, 74, 083515
Bernui A., Villela T., Wuensche C. A., Leonardi R., and Ferreira I., 2006, A&A, 454, 409
de Oliveira-Costa A., and Tegmark M., 2006, PRD, 74, 023005
Rakic A., Rasanen S., and Schwarz D. J., 2006, MNRAS, 369, L27
Copi C., Huterer D., Schwarz D., and Starkman G., 2007, PRD, 75, 023507
Babich D., and Pierpaoli E., 2008, PRD, 77, 123011
Gruppuso A., and Burigana C., 2009, JCAP, 08, 004
Cabella P. et al., 2010, MNRAS, 405, 961
Short J., and Coles P., 2010, MNRAS, 401, 2202
Aluri P. K., Samal P. K., Jain P., and Ralston J. P., 2011, MNRAS, 414, 1032
Cruz M., Vielva P., Martinez-Gonzalez E., and Barreiro R. B., 2011, MNRAS, 412, 2383
Aluri P. K., and Jain P., 2012, MNRAS, 419, 3378
Lacasa F., Aghanim N., Kunz M., and Frommert M., 2012, MNRAS, 421, 1982
Chingangbam P., and Park C., 2013, JCAP, 02, 031
Kovacs A., Szapudi I., and Frei Z., 2013, Astronomische Nachrichten, 334, 1020
Liu H., Mertsch P., and Sarkar S., 2014, ApJ, 789, L29
Novaes C. P., Bernui A., Ferreira I. S., and Wuensche C. A., 2014, JCAP, 01, 018
Rassat A., Starck J.-L., Paykari P., Sureau F., and Bobin J., 2014, JCAP, 08, 006

- Axelsson M., Ihle H. T., Scodeller S. and Hansen F. K., 2015, *A&A*, 578, A44
- Tegmark M., de Oliveira-Costa A., and Hamilton A.J., 2003, *PRD*, 68, 123523
- Eriksen H. K., Banday A. J., Gorski K. M., and Lilje P. B., 2004, *ApJ*, 612, 633
- Leach S. M. et al., 2008, *A&A*, 491, 597
- Saha R., 2011, *ApJ*, 739, L56
- Bennett C. L. et al., 2003, *ApJS*, 148, 97
- Afshordi N., Loh Y.-S., and Strauss M. A., 2004, *PRD*, 69, 083524
- Coles P., Dineen P., Earl J. and Wright D., 2004, *MNRAS*, 350, 989
- Dineen P., and Coles P., 2004, *MNRAS*, 347, 52
- Bernardi G., Carretti E., Fabbri R., Sbarra C., and Cortiglioni S., 2005, *MNRAS*, 364, L5
- Naselsky P. D., Chiang L.-Y., Novikov I. D., and Verkhodanov O. V., 2005, *IJMPD*, 14, 1273
- Alvarez M. A., Komatsu E., Dore O., and Shapiro P. R., 2006, *ApJ*, 647, 840
- Rassat A., Land K., Lahav O., and Abdalla F. B., 2007, *MNRAS*, 377, 1085
- Land K., and Slosar A., 2007, *PRD*, 76, 087301
- Sarkar T. G., Datta K. K., and Bharadwaj S., 2009, *JCAP*, 08, 019
- Hernandez-Monteagudo C., 2010, *A&A*, 520, A101
- Lopez-Corredoira M., Labini F. S., and Betancort-Rijo J., 2010, *A&A*, 513, A3
- Naselsky P. D. et al., 2010, *Astrophysical Bulletin*, 65, 101
- Sawangwit U. et al., 2010, *MNRAS*, 402, 2228
- Ilic S., Douspis M., Langer M., Penin A., and Lagache G., 2011, *MNRAS*, 416, 2688
- Taburet N., Hernandez-Monteagudo C., Aghanim N., Douspis M., and Sunyaev R., 2011, *MNRAS*, 418, 2207
- Hansen M. et al., 2012, *MNRAS*, 426, 57
- Hansen M. et al., 2012, *MNRAS*, 426, 57
- Wibig T. and Wolfendale A. W., 2015, *MNRAS*, 448, 1030
- Aluri P. K., *Large scale anomalies in the Cosmic Microwave Background Radiation*, Ph.D. thesis submitted to Department of Physics, IIT Kanpur, India in December 2011
- Finkbeiner D. P., Davis M., and Schlegel D. J., 1999, *ApJ*, 524, 867
- Finkbeiner D. P., 2003, *ApJS*, 146, 407
- Haslam C. G. T., Salter C. J., Stoffel H., and Wilson W. E., 1982, *A&AS*, 47, 1
- Adam R. et al., 2015, arXiv:1502.01588
- Hinshaw G. F. et al., 2013, *ApJS*, 208, 19H
- Lewis A., Challinor A. and Lasenby A., 2000, *ApJ*, 538, 473
- Howlett C., Lewis A., Hall A. and Challinor A., 2012, *JCAP*, 04, 027
- Eriksen H. K. et al., 2008, *ApJ*, 676, 10
- Adam R. et al., 2015, arXiv:1502.05956
- Vielva P., Martinez-Gonzalez E., Barreiro R. B., Sanz J. L., and Cayon L., 2004, *ApJ*, 609, 22
- Tomita K., 2005, *PRD*, 72, 103506
- Cruz M., Tucci M., Martinez-Gonzalez E., and Vielva P., 2006, *MNRAS*, 369, 57
- Inoue K. I., and Silk J., 2007, *ApJ*, 664, 650
- Rudnick L., Brown S., and Williams L. R., 2007, *ApJ*, 671, 40
- Cruz M. et al., 2008, *MNRAS*, 390, 913
- Bernui A., 2009, *PRD*, 80, 123010
- Smith K. M., and Huterer D., 2010, *MNRAS*, 403, 2
- Zhang R., and Huterer D., 2010, *Astroparticle Physics*, 33, 69
- Afshordi N., Slosar A., and Wang Y., 2011, *JCAP*, 01, 019